PPPL-5270

Kinetic neoclassical calculations of impurity radiation profiles

D.P. Stotler, D.J. Battagliaa, R. Hager, K. Kim, T. Koskela, G. Park, M.L. Reinke

July 2016

Prepared for the U.S.Department of Energy under Contract DE-AC02-09CH11466.

Princeton Plasma Physics Laboratory
Report Disclaimers

Full Legal Disclaimer

This report was prepared as an account of work sponsored by an agency of the United States Government. Neither the United States Government nor any agency thereof, nor any of their employees, nor any of their contractors, subcontractors or their employees, makes any warranty, express or implied, or assumes any legal liability or responsibility for the accuracy, completeness, or any third party's use or the results of such use of any information, apparatus, product, or process disclosed, or represents that its use would not infringe privately owned rights. Reference herein to any specific commercial product, process, or service by trade name, trademark, manufacturer, or otherwise, does not necessarily constitute or imply its endorsement, recommendation, or favoring by the United States Government or any agency thereof or its contractors or subcontractors. The views and opinions of authors expressed herein do not necessarily state or reflect those of the United States Government or any agency thereof.

Trademark Disclaimer

Reference herein to any specific commercial product, process, or service by trade name, trademark, manufacturer, or otherwise, does not necessarily constitute or imply its endorsement, recommendation, or favoring by the United States Government or any agency thereof or its contractors or subcontractors.

PPPL Report Availability

Princeton Plasma Physics Laboratory:

http://www.pppl.gov/techreports.cfm

Office of Scientific and Technical Information (OSTI):

http://www.osti.gov/scitech/

Related Links:

U.S. Department of Energy

U.S. Department of Energy Office of Science

U.S. Department of Energy Office of Fusion Energy Sciences

Kinetic neoclassical calculations of impurity radiation profiles

D. P. Stotler[a,*], D. J. Battaglia[a], R. Hager[a], K. Kim[b], T. Koskela[c],
and G. Park[d], M. L. Reinke[e],

[a]*Princeton Plasma Physics Laboratory, Princeton University, P. O. Box 451,*
Princeton, NJ 08543-0451, USA

[b]*KAIST, Daejeon, South Korea*

[c]*Lawrence Berkeley National Laboratory, Berkeley, CA 94720 USA*

[d]*National Fusion Research Institute, Daejeon, South Korea*

[e]*Oak Ridge National Laboratory, P. O. Box 2008, Oak Ridge, TN 37831, USA*

Modifications of the drift-kinetic transport code XGC0 to include the transport, ionization, and recombination of individual charge states, as well as the associated radiation, are described. The code is first applied to a simulation of an NSTX H-mode discharge with carbon impurity to demonstrate the approach to coronal equilibrium. The effects of neoclassical phenomena on the radiated power profile are examined sequentially through the activation of individual physics modules in the code. Orbit squeezing and the neoclassical inward pinch result in increased radiation for temperatures above a few hundred eV and changes to the ratios of charge state emissions at a given electron temperature. Analogous simulations with a neon impurity yield qualitatively similar results.

Keywords: Neoclassical Transport, Impurity Radiation, Coronal Equilibrium, Kinetic Simulation, Particle-In-Cell, Spherical Torus

[*]Corresponding and presenting author

Email address: `dstotler@pppl.gov` (D. P. Stotler)

1 Introduction

Extrapolation of empirical transport trends predicts that to maintain divertor heat loads at tolerable levels, ITER will need to radiate 80% of its total input power, with roughly 30% coming from the core [1]. The requirements for DEMO are more severe yet, with a total radiated fraction of $\sim 90\%$ and $\sim 50\%$ from the core [2]. An understanding of the spatial distribution of impurity radiation in the edge and scrape-off layer (SOL) of tokamaks is needed to ensure that such predictions are as accurate as possible. While existing diagnostics techniques, such as resistive bolometry, can determine the integrated amount of power radiated, they have very poor spatial resolution. The need for better spatial resolution is especially critical in the steep gradient region of the H-mode pedestal and near the X-point where shifts of a cm or a few mm can dramatically alter the division of the cooling between closed and open flux surfaces.

The bulk of the tokamak impurity transport and radiation modeling to date has been carried out via fluid plasma codes solving the Braginskii equations [3, 4, 5]. While these do provide spatially resolved, and time dependent profiles of the impurity charge state distributions and the associated radiation, they inherently miss the kinetic and non-local neoclassical effects on ion transport that can be dominant [6, 7] in the steep pedestal region of H-mode plasmas.

The full-f, drift-kinetic, multi-species, particle-in-cell (PIC) transport code XGC0 [8] has been applied previously to examine kinetic and non-local neoclassical effects on the main ion plasma [7, 8], including self-consistently determined radial electric field and sheath potential to ensure ambipolarity, as well as neutral recycling and ionization [9]. An acknowledged limitation of the work reported in [7] is that the carbon impurity had a fixed charge (6+) and the associated radiative cooling was not consistently determined.

We describe here the extension of XGC0 to resolve the individual impurity charge states and to track the associated radiation and electron cooling / heating, taking another step towards a nearly first principles tool for fusion plasma simulation. Generalized collisional radiative (GCR) rates are used for all atomic physics processes [10, 11]. Starting with input plasma profiles based on an NSTX H-mode discharge, the deuterium ion and impurity species are evolved in time towards neoclassical transport equilibrium, including a recycling source determined from consistent neutral deuterium and impurity density profiles. To facilitate comparison of the spatial distribution of the radiated power with that obtained from coronal equilibrium (CE), the electron density and temperature profiles are held fixed throughout.

Section 2 describes the implementation of impurity ionization and recombination into XGC0 and the associated assumptions. That the resulting model is consistent with coronal equilibrium is demonstrated in Sec. 3. The effects of neoclassical phenomena on the impurity charge state distribution and radiation profile are detailed in Sec. 4. Finally, in Sec. 5, we summarize and discuss related work planned for the future.

2 Implementation of Multiple Charge States in XGC0

The XGC family of codes began with the five dimensional (three space, two velocity), full-f, drift-kinetic PIC code described in [8]. That code and all subsequent versions of XGC0 have at their core a particle pushing algorithm that integrates the Hamiltonian equations of motion [8, 12] in time for a set of marker particles representing the ion (and electron, when included) guiding centers. The algorithm is designed to work efficiently and accurately in a magnetic separatrix geometry based on a numerically specified equilibrium, allowing plasma transport to be simulated from the magnetic axis to the material surfaces. A second critical component of XGC0 is the temporal evolution of the radial electric field via Ampere's law averaged over a closed flux surface [8]. The principal effect of the electric field is to increase the energy thresholds for X-loss [13, 8] and orbit loss [14] enough that the associated sinks of energetic main ions can be offset by the inward pinch [15, 16] of colder ions and impurities, maintaining ambipolar plasma transport across the separatrix. Improvements made to XGC0 since the original version include: realistic recycling [9], kinetic electrons, impurity ions, conserving linear Fokker-Planck operator, diffusive anomalous transport, logical sheath [7] and three-dimensional magnetic perturbations [17].

The variety of problems that can be studied with XGC0 has been limited by the fixed charge state of the impurity species and the relatively simple models available for describing impurity radiation [18, 19]. We relax these limitations by including the particle charge state as an additional phase space parameter that can vary in time; this is preferable to the alternative of representing each charge state as a distinct particle "species". For low-Z elements, such as carbon or neon, all charge states can be readily included in the simulations. Treating high-Z species, e.g., molybdenum or tungsten, will likely require the use of "bundled" representations of the atom's electronic structure [20]. Our implementation allows for this possibility by specifying the charge states associated with each impurity species with an array of arbitrary length.

The temporal evolution of the particle charge states via electron impact ionization and recombination is effected by a Monte Carlo algorithm directly analogous to that used in simulating the ionization of neutral particles [8, 9]. Generalized collisional radiative rates (metastable unresolved) for these processes, as well as the associated electron cooling and heating rates, have been extracted from the ADAS database [10] and made accessible to XGC0 via a new interface to the DEGAS 2 neutral transport code [21] developed expressly for this purpose. Since the electron density and temperature profiles are held fixed in the present work, we defer to a future publication a description of our approach to incorporating the effects of ionization and recombination on the electron population.

Note that XGC0, like most transport codes, works internally with the rate at which electrons lose or gain energy as impurities are being ionized and recombined. To show how this relates to the more experimentally relevant radiated power, we first write the equivalent time rate of change of the density of impurity charge state q as:

$$\frac{dn_q}{dt} = -n_q n_e S_q + n_{q+1} n_e R_{q+1} + n_{q-1} n_e S_{q-1} - n_q n_e R_q, \tag{1}$$

with $q = 1 \to Z$; S_0 is the rate at which neutral impurities are ionized, and $R_{Z+1} = S_Z = 0$. All impurity transport phenomena are effectively represented by the total derivative on the left-hand side. The S_q and R_q are the GCR rates, "SCD" and "ACD" in ADAS nomenclature, respectively. In terms of these quantities, the electron cooling power associated with charge state q is then

$$P_{\mathrm{cool},q} = E_{\mathrm{ion},q}(n_q n_e S_q - n_{q+1} n_e R_{q+1}) + n_q n_e P_{\mathrm{ion},q} + n_{q+1} n_e P_{\mathrm{rec},q+1}, \qquad (2)$$

where $q = 1 \to Z - 1$ (losses associated with neutral ionization are compiled on a different mesh in XGC-0 and are not discussed here), and $E_{\mathrm{ion},q}$ is the energy required to ionize the $+q$ ion. $P_{\mathrm{ion},q}$ ("PLT" in ADAS) and $P_{\mathrm{rec},q+1}$ ("PRB') are the total rates of line emission associated with ionization and recombination, respectively, between charge states q and $q+1$. Equation (2) is equivalent to Eq. (27) of [11], although demonstrating the correspondence requires some manipulation of terms. The corresponding expression for the radiated power is:

$$P_{\mathrm{rad},q} = n_q n_e P_{\mathrm{ion},q} + n_{q+1} n_e P_{\mathrm{rec},q+1}. \qquad (3)$$

In equilibrium, $n_q/n_{q+1} = R_{q+1}/S_q \Rightarrow P_{\mathrm{cool},q} = P_{\mathrm{rad},q}$. Since all of the data presented below, apart from the earliest time steps of the run described in Sec. 3, are at or relatively close to equilibrium, we treat the terms "electron cooling" and "radiated power" as interchangeable. Namely, the plots depict the electron cooling compiled by the code, but we will refer to it as the radiated power.

Related quantities include the total impurity density, $n_I = \sum_{q=1}^{Z} n_q$, total "radiated" power:

$$P_{\mathrm{rad}} \equiv \sum_{q=1}^{Z-1} P_{\mathrm{cool},q}, \tag{4}$$

and, as in [22, 23, 24], the effective "radiated" power per electron and impurity ion:

$$L_{\mathrm{rad}} \equiv P_{\mathrm{cool}}/(n_e n_I). \tag{5}$$

The electron densities and temperatures required to evaluate the GCR rates are compiled on a 2-D mesh that, on closed flux surfaces, coincides with that used by the linear Fokker-Planck collision operator. For all simulations described here, this mesh consists of 50 cells spaced uniformly in poloidal flux between $\psi_n \equiv \psi/\psi_{\mathrm{sep}} = 0.4$ and the separatrix, and four divisions uniform in poloidal angle, with the first centered about the outboard midplane. The SOL regions above and below the X-point are represented by five cells each, up to $\psi_n = 1.05$. The entirety of the lower private flux region (PFR) is incorporated into one additional cell. All relevant output data are compiled on this same mesh, although the results shown here have been reduced to one dimension by poloidal averaging. As with previous XGC0 applications [9, 25, 7], our emphasis will be on phenomena in the confined plasma, with relatively simple models of open field line behavior to facilitate the specification of boundary conditions. More detailed treatment of SOL and PFR physics awaits the development of similar impurity transport capabilities in the XGCa code [26, 27].

The source of impurity ions in previous XGC0 versions was assumed proportional to the source of (main) deuterium ions arising from the ionization of atoms generated by recycling [7]. The neutral density profile used for this purpose is the result of a separate kinetic, Monte Carlo calculation performed on a fluid plasma background. The spatial variation of the neutral source for that process is taken to be proportional to flux of ions lost to the walls and divertor. Here, we extend this model by compiling separate neutral atom density profiles for each impurity species and then use them to determine the 1+ ion particle source via the ADAS neutral ionization rate and the same Monte Carlo collision algorithm used for deuterium.

Presently, the poloidal distribution of the impurity neutral source is equal to that of the deuterium neutrals. As in the deuterium neutral transport model, the neutral source is characterized by a specified recycling rate, 99% here, and a 3 eV thermal energy distribution. Only ionization (no charge exchange) is considered in the interactions of the neutral impurity atoms with the plasma. DEGAS 2 will ultimately be used to provide a more realistic characterization of the impurity source, e.g., via sputtering and neutral-plasma interactions.

XGC0 impurity simulations utilize a linear Fokker-Planck collision operator that explicitly conserves mass, momentum, and energy. The outermost loop of the collision operation is over species; each serves as a "background" for a standard Monte Carlo collision operation [28] for all other "test" species, including self-collisions. To generalize the procedure for multiple charge states, inner loops over charge states have been added to both loops over "background" and "test" species. The energy and momentum exchanged in the Monte Carlo collisions is tabulated as a function of space, as well as the "test" species and charge state. In the second stage of the linearized collision process, the "restoring" force of the Monte Carlo collisions on the background particles is applied using expressions in [29]. A third stage enforces particle, momentum, and energy conservation via a technique similar to that of [30].

If the density of a particular "background" charge state is zero in a mesh cell or if there are too few particles (< 100) to accurately compute a temperature, the collision operations in that cell are bypassed completely for that charge state. Additional numerical difficulties may arise for low, but non-zero, background density states. As a first step towards their mitigation, the global energy exchange in the Monte Carlo collisions is summed over test species and compared with the corresponding sum for the D^+ background. If the ratio is $< 1\%$, the second and third stages of the collision routine are bypassed. In practice, the routine is not entirely robust, and its conservation properties are poorer than its operation with fixed charge state impurities. The resulting error in a simulation is quantified below. Continued refinements in the model and its verification via conservation and equilibration tests [26] will be discussed in a subsequent publication.

3 Approach to Coronal Equilibrium

To verify the ionization-recombination model and to provide a starting point for quantifying the effects of neoclassical phenomena, we demonstrate the approach to coronal equilibrium starting from singly charged carbon ions. Note that the code possesses no method for initializing the simulation with only neutral impurity atoms. To make contact with standard references on the topic, e.g., [22, 23, 24], we disable all physical processes in the code apart from ionization and recombination; the simulation particles are *not* moving.

The particular ADAS files used are from the “96” set and are dated November 4, 1999.

The magnetic equilibrium and plasma profiles used are based on NSTX H-mode shot 139047 at 580 ms (Fig. 1); they are similar to the ones analyzed in [31], although no initial toroidal rotation is specified for these simulations. Again, the electron density and temperature profiles are held fixed to allow the effects of neoclassical phenomena on the impurity ions to be elucidated.

This simulation is run in three parts, with the time step increasing a factor of ten with each restart; the total time elapsed is 22 ms. The volume integrated L_{rad} is plotted in Fig. 2. The times used to label the curves are “normalized” by the electron density at the core boundary, $n_{\mathrm{core}} = 6.8 \times 10^{19}$ m^{-3}. This situation is not directly analogous to those in [22, 23] since n_e varies with T_e across our simulation’s radial profile. Nonetheless, the simulated curves converge towards the equilibrium result, computed directly from the ADAS rates, at roughly the same pace as in [23].

4 Neoclassical Effects on Radiation Profile

The simulations discussed in this section either begin with the near-equilibrium state obtained above or with a CE charge state distribution computed directly from the ADAS rates; the results of the two approaches are similar.

We first enable the ion particle push to assess the effect of orbit width on L_{rad}. Carbon ion orbits in the steep gradient region have widths on the order of $\Delta\psi/\psi_{\mathrm{sep}} = 0.02$, comparable to the electron density and temperature gradient scale lengths. These orbit widths are reduced by the “orbit squeezing”

[8] associated with the radial electric field.

The effect of non-zero orbit width is incorporated into the initial coronal equilibrium since the ion starting positions are sampled at all points along the orbits. The orbital periods in the steep gradient region are on the order of 10^{-4} s, much shorter than the relevant recombination ($\sim 10^{-2}$ s) and ionization ($> 10^{-3}$ s) times. Consequently, the ions do not undergo noticeable change in charge state density, even though they sample a range of density and temperature values.

The initial state of this simulation has no electric field so that orbit squeezing does not take effect until the radial electric field has been established. The squeezing not only reduces the orbit widths, but also shifts them inward, on average, in the steep gradient region. The relative increases in the C^{4+} and C^{5+} fractions result in enhanced $L_{\rm rad}$ around $T_e \simeq 200$ eV ($\psi_n \simeq 0.93$) early in the simulation ($t = 1.4 \times 10^{-4}$ s; dashed blue curves in Fig. 3). The charge state distribution eventually adjusts to the shift, and the effective $L_{\rm rad}$ decays towards the equilibrium result ($t = 4.6 \times 10^{-3}$ s; solid blue curves).

We next incorporate a source of impurities, the aforementioned 99% recycling rate that replaces the ions lost to the walls by X- and orbit loss. The initial impact of the resulting influx of low charge state ions (dashed green curves in Fig. 3) is large with significant increases in $L_{\rm rad}$ for $T_e < 200$ eV. However, the recycled ions are too low in energy to enter the loss cone so that this effect also decays for $T_e \geq 30$ eV, and the effective $L_{\rm rad}$ again approaches the equilibrium value (solid green curves). The elevated values below 30 eV represent ongoing recycling in the SOL.

The inclusion of collisions via the linearized Fokker-Planck operator in-

inward shifts of the contributions from $3 \leftrightarrow 4$ on up. Note that on this scale, the CE $1 \leftrightarrow 2$ and $2 \leftrightarrow 3$ components are essentially zero and are not shown. In the non-equilibrium simulation, X- and orbit loss and the compensating recycling source cause them to no longer be negligible. The absolute power associated with each charge state at a given T_e is only quantitatively different in the two situations. However, the *ratios* of the powers in two charge states, more readily measured spectroscopically, change dramatically. This result provides an effective basis for identifying the presence of these phenomena in experimental data.

We have performed an analogous simulation with neon impurity for comparison. The initial density was set to half of the carbon density in Fig. 1, and a CE charge state distribution was used. The ADAS "96" files were dated June 11, 2014. As with carbon, the effective L_{rad} diverges from CE very early in the simulation, but not for $T_e < 30$ eV or $T_e > 300$ eV ($t = 0.2$ ms; dashed cyan curve in Fig. 3). As the calculation progresses, and the neon ions are pinched in, L_{rad} is enhanced by almost a factor of two in the core of the simulation. Again due to the weighting by the densities, this increase carries over into the total radiated power, which is 65% larger than the CE value (1.58 MW vs. 0.95 MW), and into the radiation density, Fig. 4. The shifts in the individual charge state contributions, Fig. 6 are reminiscent of those seen for carbon.

troduces pitch angle scattering of the carbon ions off of deuterium and other carbon ions, moving some ions from confined to loss orbits and resulting in a nearly steady state enhancement of the radiation at lower electron temperatures (orange curves in Fig. 3). Note that anomalous transport, which will be included in discharge-specific simulations (as in [7]), provides another mechanism for moving ions onto loss orbits. The neoclassical inward pinch acts to boost the population of C^{4+} and C^{5+} in the core region of the simulation, increasing the effective $L_{\rm rad}$ for $T_e > 250$ eV in Fig. 3. That the inward pinch now carries a non-trivial distribution of carbon charge states represents an improvement in the determination of the radial ion current and thus in the radial electric field calculation relative to that of previous XGC0 versions.

The numerical problems with the Fokker-Planck collision routine referred to in Sec. 2 result in a 2% gain in the total carbon population over the 50,000 steps of the simulation, a deviation too small to impact our conclusions. An analogous simulation with fixed (+6) charge state carbon ions yields essentially the same final density, flow velocity, and temperature profiles.

Incorporating neoclassical phenomena into the simulation results in a 36% increase in the radiated power relative over that of CE (0.24 MW and 0.18 MW, respectively). The bulk of this change arises for $\psi_n < 0.9$ even though the enhancements in $L_{\rm rad}$ are greater at lower temperatures simply because the densities are much lower outside the pedestal, as can be seen in a plot of the radiation density, $n_e n_C L_{\rm rad}$, in Fig. 4. This figure depicts the same trend seen in Fig. 3, but reflects the weighting by the densities.

The radiated power profile broken down by charge state as in Eq. (2) is compared with the CE result in Fig. 5. The neoclassical effects result in

5 Conclusions

We have described the incorporation of impurity ionization and recombination into the drift-kinetic transport code XGC0. We ran this code with an NSTX H-mode plasma to illustrate the effects of neoclassical phenomena, including orbit squeezing, ion X- and orbit loss, neutral recycling, and inward pinch, on the impurity charge state distributions and radiation profile. The principal result for a carbon impurity is an increase in the effective radiation per electron and ion, L_{rad}, for virtually all electron temperatures in the simulated plasma. The enhancement for $T_e > 250$ eV associated with the inward pinch acting on C^{4+} and C^{5+} ions results in a 36% increase in total radiated power relative to the value obtained with a coronal equilibrium charge state distribution. The ratios of the power radiated by two charge states at a given electron temperature are even more strongly impacted by these effects. An analogous simulation with neon impurity yields qualitatively similar effects.

XGC0 simulations including kinetic electrons, and the effects of impurity radiation on their energy balance, are currently underway and will be reported in a future publication. The inclusion of diffusive anomalous transport and core particle, momentum, and energy sources will permit detailed modeling of individual experimental discharges, as in [7]. The next principal improvement to the model is the replacement of the XGC0 neutral transport model with DEGAS 2, a straightforward extension of the method described in [9]. This will provide improved spatial resolution along flux surfaces, allow the incorporation of other atomic physics processes, e.g., charge exchange of carbon ions with neutral hydrogen, and permit the use of more realistic plasma-material interactions and sputtering sources.

Acknowledgments

This work is supported by U.S. DOE Contracts DE-AC02-09CH11466 (PPPL) and DE-AC05-00OR22725 (ORNL). Additional support was provided through the Scientific Discovery through Advanced Computing (SciDAC) program funded by the U.S. DOE Office of Advanced Scientific Computing Research and the Office of Fusion Energy Sciences. Some of the work described here was carried out on resources of the National Energy Research Scientific Computing Center, a U.S. DOE Office of Science User Facility supported by the Office of Science of the U.S. DOE under Contract No. DE-AC02-05CH11231. The digital data for this paper can be found in `http://arks.princeton.edu/ark:/88435/dsp018p58pg29j`.

References

[1] A. Loarte et al., Phys. Plasmas 18 (2011) 056105.

[2] R. P. Wenninger et al., Nucl. Fusion 54 (2014) 114003.

[3] M. Groth et al., J. Nucl. Mater. 415 (2011) S530.

[4] M. Wischmeier et al., J. Nucl. Mater. 415 (2011) S523.

[5] C. Guillemaut et al., J. Nucl. Mater. 438 (2013) S638.

[6] C. G. Wrench et al., in: 38th EPS Conference on Plasma Physics 2011, EPS 2011 - Europhysics Conference Abstrats, Vol. 35, 2011, pp. 1800–1802, 38th EPS Conference on Plasma Physics 2011, EPS 2011, Strasbourg, France, 27 June - 1 July 2011.

[7] D. J. Battaglia et al., Phys. Plasmas 21 (2014) 072508.

[8] C. S. Chang et al., Phys. Plasmas 11 (2004) 2649.

[9] D. P. Stotler et al., Comput. Sci. Disc. 6 (2013) 015006.

[10] H. P. Summers, The adas user manual, version 2.6, `http://www.adas.ac.uk` (2002).

[11] H. P. Summers et al., Plasma Phys. Control. Fusion 48 (2006) 263.

[12] M. F. Adams et al., J. Phys.: Conf. Ser. 180 (2009) 012036.

[13] C. S. Chang et al., Phys. Plasmas 9 (2002) 3884.

[14] K. C. Shaing et al., Phys. Rev. Lett. 63 (1989) 2369.

[15] F. L. Hinton, R. D. Hazeltine, Rev. Mod. Phys. 48 (1976) 239.

[16] P. Helander, D. J. Sigmar, Collisional transport in magnetized plasmas, Cambridge University Press, New York, 2002.

[17] G. Park et al., Phys. Plasmas 17 (2010) 102503.

[18] D. E. Post et al., At. Data Nucl. Data Tables 20 (1977) 397.

[19] R. A. Hulse, Nucl. Tech. / Fusion 3 (1983) 259.

[20] X. Bonnin, D. Coster, J. Nucl. Mater. 415 (2011) S488.

[21] D. P. Stotler, C. F. F. Karney, Contrib. Plasma Phys. 34 (1994) 392.

[22] P. G. Carolan, V. A. Piotrowicz, Plasma Phys. 25 (1983) 1065.

[23] D. E. Post, J. Nucl. Mater. 220–222 (1995) 143.

[24] A. Kallenbach et al., Plasma Phys. Control. Fusion 55 (2013) 124041.

[25] D. P. Stotler et al., J. Nucl. Mater. 438 (2013) S1275.

[26] R. Hager et al., Phys. Plasma 23 (2016) 042503.

[27] R. M. Churchill et al., Nucl. Mater. Energy (these proceedings).

[28] A. H. Boozer, G. Kuo-Petravic, Phys. Fluids 24 (1981) 851.

[29] S. P. Hirshman, D. J. Sigmar, Phys. Fluids 19 (1976) 1532.

[30] W. X. Wang et al., Plasma Phys. Control. Fusion 41 (1999) 1091.

[31] A. Diallo et al., Nucl. Fusion 53 (2013) 093026.

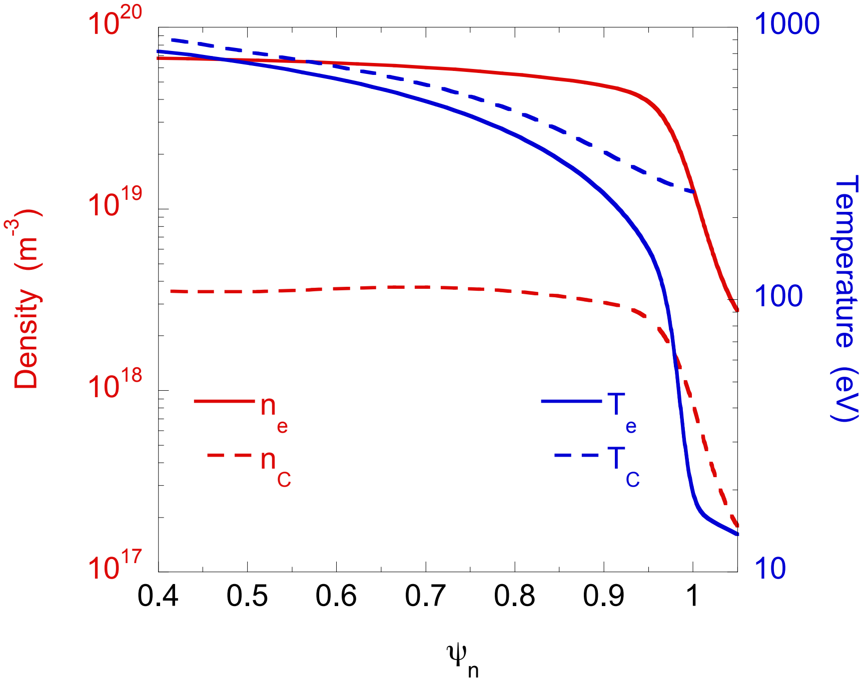

Figure 1: Temperature (right axis) and density (left axis) profiles for electrons (solid curves) and carbon (dashed curves) input to XGC0, similar to NSTX H-mode discharge 139047 [31].

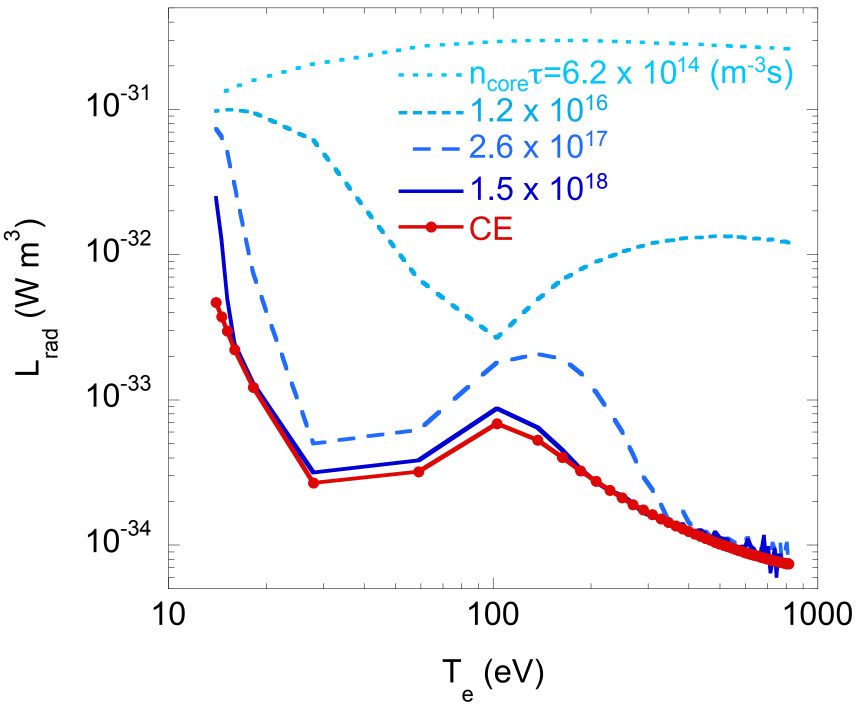

Figure 2: Radiation rates per carbon ion and per electron plotted as a function of the electron temperatures in the simulation to obtain curves analogous to those in [22], [23], and [24]. The "Equilibrium" curve is computed directly from the ADAS rates evaluated at each T_e, n_e in the simulation. The blue curves represent different time steps, τ, during the run. The curve labels show the normalized time [23] obtained as the product of τ with n_e at the simulation's core boundary (6.8×10^{19} m^{-3}); the density at the outermost surface is roughly a factor of 20 smaller (3.1×10^{18} m^{-3}).

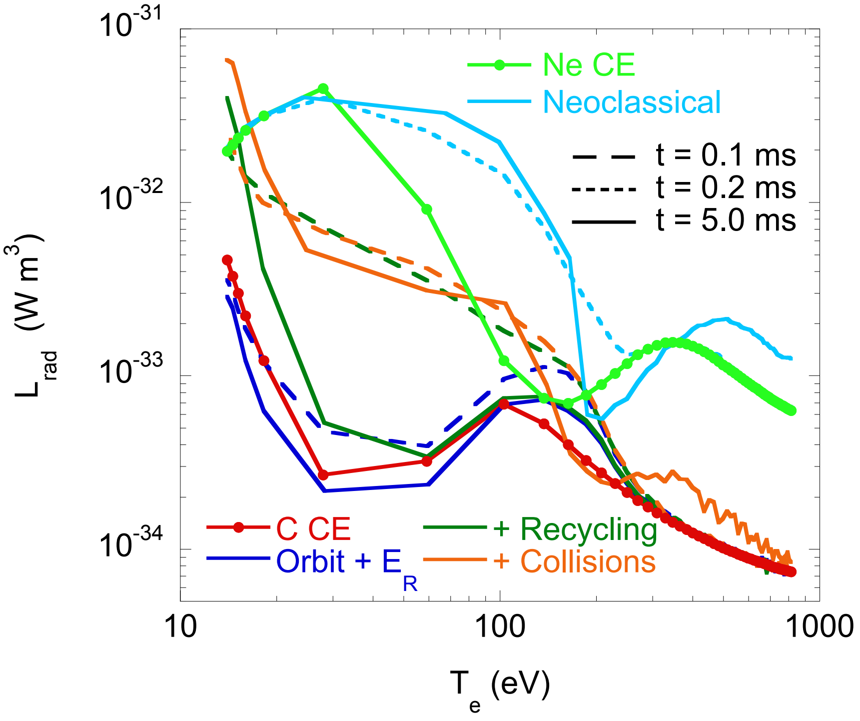

Figure 3: Effects of neoclassical phenomena on L_{rad}. The equilibrium result is as in Fig. 2. The blue curves are from two points in time in a run in which the carbon and deuterium ions orbits are followed and a self-consistent radial electric field is computed. The result of adding neutral recycling for both species is depicted by the green curves. Including collisions results in the orange curves. An analogous simulation with all processes in effect is run with a neon impurity, yielding the cyan curves. The corresponding coronal value is shown in light green.

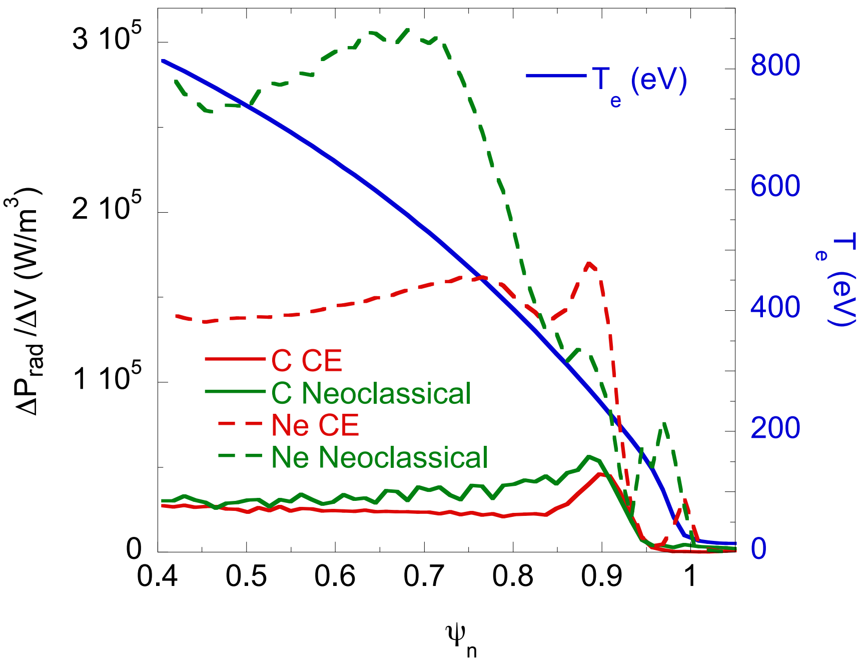

Figure 4: Radial profiles of the integrated radiation density as function of the normalized poloidal flux for the equilibrium (red) and neoclassical (green) cases in the runs with carbon (red) and neon (green) impurity. These profiles represent the contribution to the total radiation made by each radial cell in the mesh (ΔP) divided by its volume (ΔV). The T_e profile from Fig. 1 is included for reference.

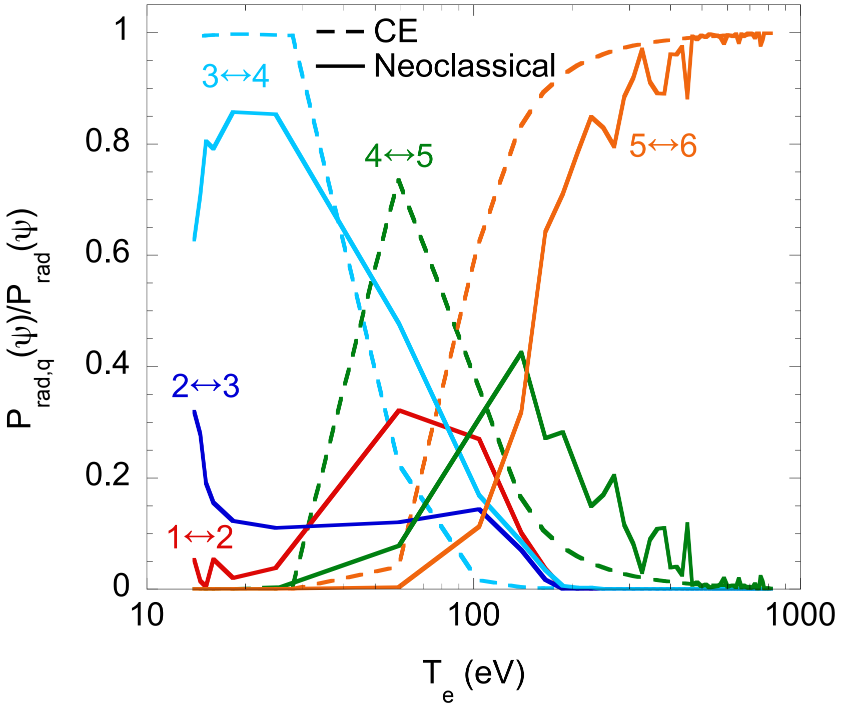

Figure 5: Relative contributions to the radiated power associated with ionization and recombination between the indicated carbon charge states at a given radial flux surface as a function of T_e there. The dashed curves ("CE") represent the equilibrium state shown in Fig. 2. The solid curves ("Neoclassical") are based on $t = 5$ ms in the "full physics" simulation. On this scale the power from the $1 \leftrightarrow 2$ and $2 \leftrightarrow 3$ equilibrium systems are effectively zero and are not shown.

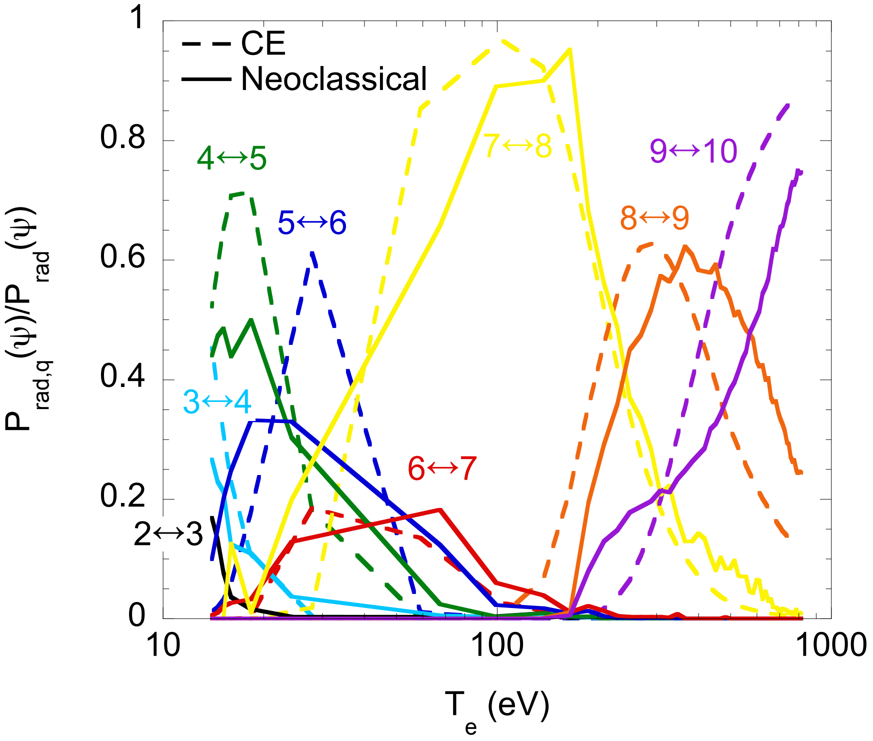

Figure 6: Relative contributions to the radiated power associated with ionization and recombination between the indicated neon charge state at a given radial flux surface as a function of T_e there. The dashed curves ("CE") represent the equilibrium state. The solid curves ("Neoclassical") are based on $t = 5$ ms in the "full physics" simulation. On this scale the power radiated by the $1 \leftrightarrow 2$ (for both simulations) and $2 \leftrightarrow 3$ (for CE) systems are effectively zero and are not shown.

P.O. Box 451, Princeton, NJ 08543
Phone: 609-243-2245
Fax: 609-243-2751

E-mail: publications@pppl.gov

Website: http://www.pppl.gov